IMPROVING METRICS FOR SATELLITE ANOMALY DETECTION: A COMPARATIVE ANALYSIS OF CURVILINEAR STATE REPRESENTATIONS

Jose M. Montilla[1], Jan A. Siminski[2], and Rafael Vazquez[1]

[1] *Universidad de Sevilla, Escuela Técnica Superior de Ingeniería, Camino de los Descubrimientos s.n 41092 Sevilla, Spain, Email: {jmontilla, rvazquez1}@us.es*

[2] *Space Debris Office, ESA/ESOC, 64293 Darmstadt, Germany, Email: jan.siminski@esa.int*

ABSTRACT

Reliable uncertainty propagation is crucial for satellite maneuver detection, particularly when using Gaussian-based anomaly metrics like the k^2, or squared Mahalanobis distance. Traditional Cartesian coordinates lose Gaussianity over time, limiting prediction accuracy. This study compares Cartesian, Modified Equidistant Cylindrical (EQCM), and Generalized Equinoctial Orbital Elements (GEqOE) representations for maintaining Gaussianity in uncertainty propagation. Using both linear methods and the Unscented Transform (UT), we assess uncertainty realism against Monte Carlo samples. Results show EQCM and GEqOE, especially with UT, significantly improve the quality of Gaussian-based uncertainty representation. Additionally, enhancing Initial Orbit Determination (IOD) with UT and Taylor algebra refines uncertainty realism of single track radar-based estimations, boosting the sensitivity and robustness of maneuver detection. The k^2 metric is evaluated across synthetic scenarios representative of operational uncertainties. This study provides practical guidelines for selecting state representations and propagation methods to optimize accuracy and reliability in satellite anomaly detection.

Keywords: Mahalanobis Distance; Maneuver detection.

1. INTRODUCTION

Spacecraft maneuver detection is vital to Space Surveillance and Tracking operations, essential for maintaining accurate catalogs and preventing collisions. Even centimeter-per-second orbital adjustments can invalidate state estimates, requiring reliable detection methods. This challenge is magnified in Low Earth Orbit, where limited observation windows and atmospheric drag amplify uncertainties, affecting critical functions from conjunction analysis to re-entry forecasting.

Recent research has explored reachability-based metrics and control distances, particularly for geostationary orbits [19, 3, 17, 8], demonstrating that maneuvers can be inferred by testing the feasibility of linking pre- and post-maneuver orbits with minimal propulsive cost. However, translating these concepts to LEO scenarios with a single radar track and strong perturbations remains non-trivial [15]. Effective maneuver detection demands accurate orbital uncertainty representation. Classical Cartesian coordinates distort Gaussian distributions over time [11, 20], while techniques like the Unscented Transform, Gaussian-Mixtures, and alternative state representations (equinoctial or curvilinear coordinates) better maintain covariance integrity during extended propagation [16, 9, 12, 13]. Likewise, robust Initial Orbit Determination methods for short radar tracks must address strong non-linearities when mapping measurement-space uncertainty to state-space covariance [2, 1]. Accounting for dynamical model uncertainties remains critical for realistic state uncertainty characterization in orbit determination applications [4].

In this paper, we introduce a maneuver detection metric for single-track scenarios under realistic LEO operational uncertainty. Building on a short-arc IOD method that incorporates J_2 perturbations [14], we enhance accuracy using (at least) second-order approximations to better manage the non-linear mapping between measurements and orbital elements. We assess different curvilinear coordinate systems for (i) uncertainty propagation and (ii) IOD performance from sparse radar data. Results show that optimal propagation coordinates may not yield the best IOD accuracy, underscoring the need for a joint perspective. Our experiments confirm that second-order IOD in orbital elements improves detection sensitivity for low-thrust maneuvers, balancing precision and efficiency in LEO surveillance.

The paper is organized as follows: Sections 2 and 3 present the maneuver detection scenario and the metric selected for the comparative study. Section 4 discusses propagation methods for the alternative state space representations considered, while Section 5 introduces enhanced IOD techniques to address measurement non-linearities. Section 6 validates covariance consistency and Section 7 reports experimental results on the metric. Finally, Section 8 concludes with practical implications for operational surveillance.

Proc. 9th European Conference on Space Debris, Bonn, Germany, 1–4 April 2025, published by the ESA Space Debris Office
Editors: S. Lemmens, T. Flohrer & F. Schmitz, (http://conference.sdo.esoc.esa.int, April 2025)

2. SCENARIO UNDER CONSIDERATION

In the context of this study, maneuver detection is performed under a highly constrained information environment with only a single survey radar station available. This radar has a known geodetic coordinates, a fixed antenna orientation, and a defined Field of Regard (FoR). As Resident Space Objects (RSOs) pass through its surveyed volume, the radar detects them and generates a track consisting of sequential observations. Each observation provides measurements of range ρ, azimuth Az, elevation el, and range-rate $\dot{\rho}$, all subject to known uncertainties.

Once a track has been correlated with an existing catalogue entry, always assumed here, the primary objective becomes determining whether a maneuver has taken place since the last recorded estimate[1]. This is a crucial step in the catalogue maintenance process, as detecting a maneuver directly impacts how past observational data is utilized for precise orbit determination. If a maneuver is detected, prior information becomes unreliable for future orbit determination. The detection process relies on comparing the state estimate obtained through Initial Orbit Determination (IOD) from the new radar track with the predicted state propagated from the last known catalogue entry. The statistical discrepancy between these two distributions serves as the foundation for maneuver detection in this study.

The maneuver detection scenario, represented in Figure 1, relies on two key orbital state representations: a past state estimate obtained from the catalogue and a present estimate derived from radar observations. The past state at some previous epoch t_0 is assumed to be well-characterized by a six-dimensional Gaussian distribution:

$$\mathcal{N}(\boldsymbol{x}; \boldsymbol{X}_0, \mathrm{P}_0), \tag{1}$$

where $\boldsymbol{X}_0 = [\boldsymbol{r}_0 \, \boldsymbol{v}_0]$ represents the mean state vector (position and velocity in an inertial frame), and P_0 is the associated covariance matrix. This state is propagated forward to a reference epoch t_{ref}, where it defines the predicted probability density function (PDF),

$$\mathcal{N}(\boldsymbol{x}; \boldsymbol{X}_P, \mathrm{P}_P). \tag{2}$$

Simultaneously, a new estimation of the state is obtained from the radar track at the same epoch t_{ref}, resulting in a second Gaussian distribution:

$$\mathcal{N}(\boldsymbol{x}; \boldsymbol{X}_E, \mathrm{P}_E). \tag{3}$$

The statistical comparison of these two independent distributions—$\mathcal{N}(\boldsymbol{x}; \boldsymbol{X}_P, \mathrm{P}_P)$ from propagation and $\mathcal{N}(\boldsymbol{x}; \boldsymbol{X}_E, \mathrm{P}_E)$ from IOD—forms the basis of maneuver detection in this study.

[1]The prior catalogue estimate was computed through an orbit determinatio effort that could have used any number of information sources, not limited to a single radar track. The implication is that the uncertainty of this past state is low compared to the radar-based estimation used in the metric computation.

3. MANEUVER DETECTION METRIC

If the observed object follows a purely ballistic trajectory, the estimated state $\mathcal{N}(\boldsymbol{x}; \boldsymbol{X}_E, \mathrm{P}_E)$ at t_{ref} should be statistically consistent with the propagated state $\mathcal{N}(\boldsymbol{x}; \boldsymbol{X}_P, \mathrm{P}_P)$. However, if a maneuver has occurred between t_0 and t_{ref}, the two distributions will diverge beyond what can be expected of their estimated uncertainties. To quantify this deviation, a statistical measure is required to assess the distance between the estimated and predicted distributions. This study adopts a very simple approach, the squared Mahalanobis distance, also called k^2, which accounts for both the difference in mean states and the covariance structure of the distributions:

$$k^2 = (\boldsymbol{X}_E - \boldsymbol{X}_P)^T \, \mathrm{P}^{-1} \, (\boldsymbol{X}_E - \boldsymbol{X}_P), \tag{4}$$

where the total covariance matrix is given by

$$\mathrm{P} = \mathrm{P}_E + \mathrm{P}_P. \tag{5}$$

The assumptions underpinning this detection framework are:

- The IOD-derived state $\mathcal{N}(\boldsymbol{x}; \boldsymbol{X}_E, \mathrm{P}_E)$ is an unbiased, realistic estimate of the true state, within the limits imposed by observational noise and the (typical) short track durations.
- The propagated state $\mathcal{N}(\boldsymbol{x}; \boldsymbol{X}_P, \mathrm{P}_P)$ is computed under a reasonable approximation of the real-world dynamical enviroment, resulting in a realistic representation of the expected error distribution given the problem uncertainties.
- Both distributions are statistically independent.

Under the critical assumption that both state distributions remain Gaussian after propagation and estimation, the k^2 metric follows a chi-squared distribution with six degrees of freedom in the nominal, non-maneuvered case. Meeting these criteria, it is possible to set a statistically significant threshold for the maximum expected squared Mahalanobis distance, above which a maneuver is flagged. This threshold is given by:

$$k^2_{\text{th}} = \chi^2_\nu(1 - \delta), \tag{6}$$

where $\chi^2_\nu(1 - \delta)$ is the inverse chi-squared cumulative distribution function evaluated at confidence level $(1 - \delta)$ for $\nu = 6$ degrees of freedom. The choice of δ determines the sensitivity of the detection metric, with lower values reducing false positives at the cost of reduced maneuver sensitivity.

This detection framework has two key requirements. First, at a minimum, it demands preservation of Gaussian consistency for both the propagated state $\mathcal{N}(\boldsymbol{x}; \boldsymbol{X}_P, \mathrm{P}_P)$ and the radar-derived estimate $\mathcal{N}(\boldsymbol{x}; \boldsymbol{X}_E, \mathrm{P}_E)$ throughout their respective transformations. Second, and more stringently, it requires covariance realism—not merely

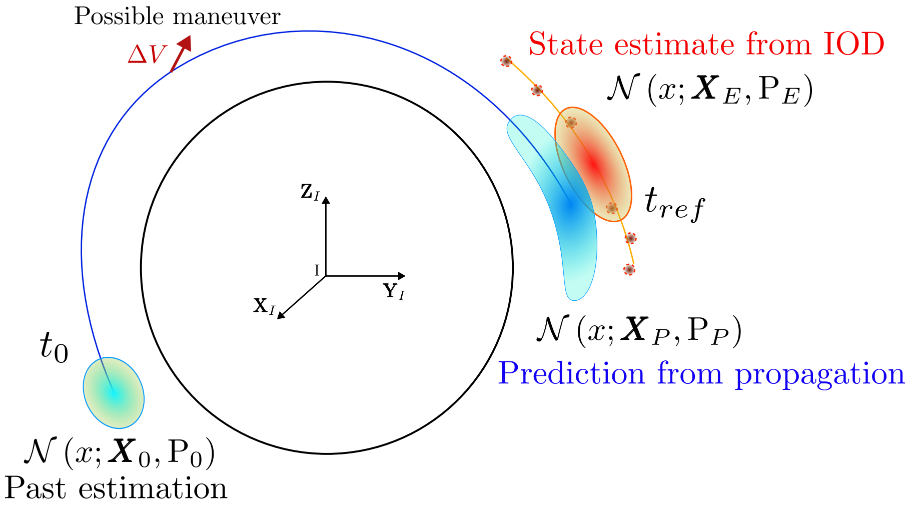

Figure 1. Maneuver detection from the track information is achieved by comparing an estimate of the orbital state $\mathcal{N}(\boldsymbol{x}; \boldsymbol{X}_E, \mathrm{P}_E)$ with the predicted PDF, characterized by $\mathcal{N}(\boldsymbol{x}; \boldsymbol{X}_P, \mathrm{P}_P)$ and obtained from a past estimation $\mathcal{N}(\boldsymbol{x}; \boldsymbol{X}_0, \mathrm{P}_0)$ at t_0. This is done with the squared Mahalanobis distance.

covariance consistency—to ensure reliable detection performance. The following sections detail how appropriate state representation, uncertainty propagation, and Initial Orbit Determination (IOD) methods are combined to meet these requirements, while highlighting the implications of achieving true covariance realism versus simple consistency.

4. COMPUTATION OF THE PREDICTION

Propagating the initial distribution $\mathcal{N}(\boldsymbol{x}; \boldsymbol{X}_0, \mathrm{P}_0)$ to t_{ref} presents two key challenges. The detection of low-magnitude maneuvers ($\sim$10 cm/s) requires high-fidelity dynamics to minimize propagation bias. Additionally, orbital non-linearities can distort the Gaussian PDF over time, potentially invalidating the k^2 metric. These challenges are addressed through two uncertainty propagation methods, each compatible with different state representations.

4.1. Uncertainty propagation methods

The propagation of uncertainty requires mapping the initial Gaussian distribution $\boldsymbol{x}_0 \sim \mathcal{N}(\boldsymbol{x}; \boldsymbol{X}_0, \mathrm{P}_0)$ at t_0 through the non-linear dynamics:

$$\dot{\boldsymbol{x}} = F(\boldsymbol{x}, t, \boldsymbol{p}), \tag{7}$$

where $\boldsymbol{p}$ represents the model parameters defining perturbation forces. The flow $\boldsymbol{x}(t) = \varphi(\boldsymbol{x}_0, t)$ of this dynamical system transforms the initial PDF into a non-Gaussian distribution at t_{ref}. However, under the assumption of limited non-linearity, this transformed distribution can be approximated as Gaussian $\boldsymbol{x}(t_{\text{ref}}) \sim \mathcal{N}(\boldsymbol{x}; \boldsymbol{X}_P, \mathrm{P}_P)$ using two different methods described below.

A comprehensive uncertainty propagation framework should account not only for the initial state uncertainty but also for uncertainties in the dynamics F and the satellite parameters $\boldsymbol{p}$. However, this work assumes high-fidelity dynamics and fixed satellite parameters, avoiding explicit modeling of process noise or parameter uncertainty. While this simplifies the computation of the solution, it potentially underestimates the true state uncertainty, particularly in cases where drag and reflectivity coefficients play a significant role [4]. The impact of these assumptions is later evaluated through simulated scenarios when both uncertainties are present but not accounted for.

The two uncertainty propagation methods applied in this study are Linear Covariance Propagation (LCP) and Unscented Transform (UT). The Linear Covariance Propagation (LCP) method propagates uncertainty by assuming local linearity around a reference trajectory. The mean state evolves according to the full non-linear dynamics:

$$\dot{\boldsymbol{x}} = F(\boldsymbol{x}, t, \boldsymbol{p}), \quad \boldsymbol{x}(t_0) = \boldsymbol{X}_0, \tag{8}$$

so that $\boldsymbol{X}_P = \varphi(\boldsymbol{X}_0, t_{\text{ref}})$. While the covariance is propagated using the state transition matrix Φ:

$$\mathrm{P}_P = \Phi_P \mathrm{P}_0 \Phi_P^T \tag{9}$$

The state transition matrix is obtained by solving the variational equations alongside the state:

$$\dot{\Phi} = \frac{\partial F}{\partial \boldsymbol{x}} \Phi, \quad \Phi(t_0) = \mathrm{I} \tag{10}$$

This captures how small deviations from the reference trajectory evolve over time. The method is computationally efficient but becomes less accurate as non-linearities grow stronger over longer propagation times.

The UT propagates uncertainty by sampling the initial distribution with a minimal set of deterministically chosen points. Given the six-dimensional state vector ($n =$

6), thirteen sigma points are selected to preserve the statistical moments:

$$\boldsymbol{X}_0^{(i)} = \boldsymbol{X}_0 \pm \sqrt{(n+\lambda)[\mathrm{P}_0]_i}, \quad i = 1, ..., n, \tag{11}$$

where $[\mathrm{P}_0]_i$ is the $i-th$ column of the matrix square root of P_0 [10]. These points are propagated individually:

$$\boldsymbol{X}_P^{(i)} = \varphi(\boldsymbol{X}_0^{(i)}, t_{ref}). \tag{12}$$

The predicted mean and covariance are then reconstructed using weighted statistics:

$$\begin{aligned}\boldsymbol{X}_P &= \sum_{i=0}^{2n} W_i^{(m)} \boldsymbol{X}_P^{(i)}, \\ \mathrm{P}_P &= \sum_{i=0}^{2n} W_i^{(c)} (\boldsymbol{X}_P^{(i)} - \boldsymbol{X}_P)(\boldsymbol{X}_P^{(i)} - \boldsymbol{X}_P)^T.\end{aligned} \tag{13}$$

The UT method captures non-linear uncertainty evolution more accurately than linear propagation while requiring only $2n+1$ propagations. The weights and scaling parameter λ are determined by three parameters: α controls the spread of sigma points, β incorporates prior knowledge of the state distribution, and κ is an additional scaling parameter. When properly tuned, these parameters ensure the UT provides a third-order accurate approximation of the mean and covariance after the non-linear transformation [6].

The choice between these methods depends on the level of non-linearity present in the problem. The following section introduces the state representation choices considered, which further influence the accuracy of uncertainty consistency.

4.2. Curvilinear state representations

Any state representation can be used for uncertainty propagation, provided the dynamics can be expressed in that frame. While propagators typically operate in standard coordinates (Cartesian, Equinoctial, Keplerian), the uncertainty can be analyzed in alternative representations through appropriate transformations.

Given the same orbital state $\boldsymbol{x}\rfloor_{\mathcal{A}}$ and $\boldsymbol{x}\rfloor_{\mathcal{B}}$ in representations $\mathcal{A}$ and $\mathcal{B}$, the transformation $\mathcal{A} \to \mathcal{B}$ and its Jacobian are:

$$\boldsymbol{x}\rfloor_{\mathcal{B}} = T_{\mathcal{A}/\mathcal{B}}(\boldsymbol{x}\rfloor_{\mathcal{A}}), \quad \mathrm{J}_{\mathcal{A}/\mathcal{B}} = \frac{\partial T_{\mathcal{A}/\mathcal{B}}}{\partial \boldsymbol{x}\rfloor_{\mathcal{A}}} \tag{14}$$

For the LCP method the transformation of the predicted distribution $\mathcal{N}(\boldsymbol{x}; \boldsymbol{X}_P, \mathrm{P}_P)$ to a different state representation is a direct transformation of the computed mean and covariance:

$$\begin{aligned}\boldsymbol{X}_P\rfloor_{\mathcal{B}} &= T_{\mathcal{A}/\mathcal{B}}(\boldsymbol{X}_P\rfloor_{\mathcal{A}}) \\ \mathrm{P}_P\rfloor_{\mathcal{B}} &= \mathrm{J}_{\mathcal{A}/\mathcal{B}}\, \mathrm{P}_P\rfloor_{\mathcal{A}}\, \mathrm{J}_{\mathcal{A}/\mathcal{B}}^T\end{aligned} \tag{15}$$

This approach assumes that the entire process applied to the initial Gaussian distribution can be linearly approximated around the reference trajectory, including transformations to a different state space. Since this is a strong assumption, the UT offers a more accurate alternative. As described in Section 4.1, propagated sigma points in (12) are further transformed using $T_{\mathcal{A}/\mathcal{B}}$ before reconstruction, ensuring that non-linear effects of the state conversion are accounted for. Notably, the UT does not require the Jacobian $\mathrm{J}_{\mathcal{A}/\mathcal{B}}$.

The proposed curvilinear state representations tested against Cartesian ($\mathcal{C}$) are the Modified Equidistant Cylindrical (EQCM, $\mathcal{E}$) [11] and the Generalized Equinoctial Orbital Elements (GEqOE, $\mathcal{G}$) [9]. EQCM has already been evaluated for this purpose in [13], while GEqOE, an alternative orbital element-based representation, is introduced here for comparative analysis. Notably, GEqOE has been previously applied in [14] for the development of an efficient J_2-corrected IOD algorithm.

The transformation and its inverse between Cartesian and GEqOE coordinates ($\mathcal{C} \leftrightarrow \mathcal{G}$), along with the associated Jacobian, are defined in [9]. However, a brief overview of these orbital elements is provided here for clarity. GEqOE generalize the classical equinoctial elements [21] by incorporating the perturbing potential $\mathscr{U}$ directly into their definition, making them well-suited for dynamical models with conservative perturbations. The formulation introduces the generalized semi-major axis a and the Laplace vector $\mu\boldsymbol{g}$, which define a non-osculating ellipse in the orbital plane. The in-plane projections of $\boldsymbol{g}$ yield the elements p_1 and p_2, which generalize the classical equinoctial elements h and k. Kepler's equation is expressed in terms of the generalized mean longitude $\mathcal{L}$, while the generalized mean motion ν is derived from the total energy, incorporating $\mathscr{U}$. Finally, the elements q_1 and q_2, analogous to the classical equinoctial elements p and q, complete the six-element GEqOE state vector:

$$\boldsymbol{\chi} = [\nu, p_1, p_2, q_1, q_2, \mathcal{L}]\,. \tag{16}$$

These are used here purely for state representation purposes, so there is no need to consider the equations of motion presented in [9].

The transformation and its inverse between Cartesian and EQCM coordinates ($\mathcal{C} \leftrightarrow \mathcal{E}$) are defined in [11], though the Jacobian of these transformations was not provided in the original work. While this Jacobian has been analytically derived in [13], the formulation has been omitted here for brevity. The EQCM representation is a modified version of the linear Hill' s frame that accounts for the reference state' s orbital eccentricity. Unlike traditional linear frames, EQCM measures distances along the Y_{EQCM} and Z_{EQCM} axes following curved paths rather than straight lines, as illustrated in Figure 2. This curvature adaptation allows uncertainty regions that appear "banana-shaped" in Cartesian space to be represented as more Gaussian-like distributions in EQCM coordinates.

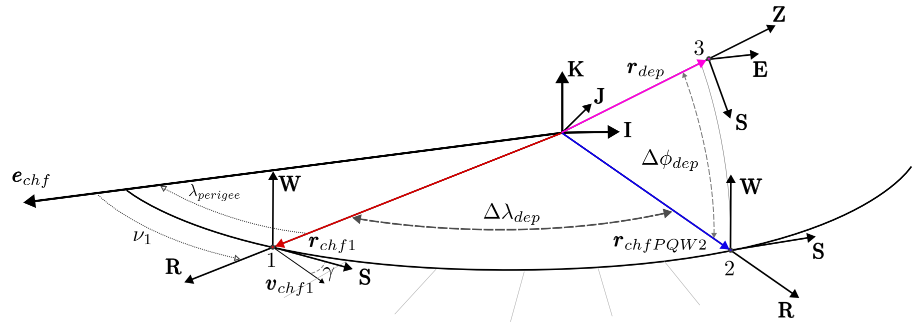

Figure 2. This is a representation of the intermediate transformations required to express the state of a deputy (or chaser) in the EQCM curvilinear frame spawned from the chief spacecraft state (point 1). The "2" intermediate local RSW frame is placed along the keplerian orbit of the chief.

5. ENHANCED INITIAL ORBIT DETERMINATION

This work leverages an algorithm for Initial Orbit Determination (IOD), published in [14], that employs a J_2-corrected dynamical model to fit various satellite state-derived variables and radar observables from a single track. The radar, characterized by a specific Field of Regard (FoR) and revisit time r_t, generates a track of N consecutive observations when a RSO passes through its FoR. The measurements include range ρ_m, azimuth Az_m, elevation el_m, and range-rate $\dot{\rho}_m$, each with an associated covariance matrix C_{z_m}.

5.1. Direct linear estimation (Traditional IOD)

The IOD process transforms radar measurements into a state estimate through an iterative linear least-squares approach. While this could accommodate any dynamical model, [14] developed an accurate short-term Taylor expansion propagator that incorporates the J_2 perturbation, which efficiently maps the radar track data (characterized by mean $\tilde{\boldsymbol{z}}$ and covariance C_z) to a state estimate:

$$(\boldsymbol{X}_E, \mathrm{P}_E) = \mathcal{F}_{\text{IOD}}(\tilde{\boldsymbol{z}}, \mathrm{C}_z), \tag{17}$$

where $\boldsymbol{X}_E = [\boldsymbol{r}, \boldsymbol{v}]$ is the estimated Cartesian state at the track' s midpoint (t_{ref}) and P_E is its covariance. While the IOD function assumes linearity during the iterative fitting process and uses first-order derivatives to approximate the output distribution, the actual transformation from measurement to state space is inherently non-linear. This limitation in uncertainty representation motivates the enhanced methods proposed in this work.

5.2. Advanced methods (UT, Taylor algebra)

To improve the uncertainty representation in IOD, two alternative approaches are proposed: the Unscented Transform and Taylor algebra. The UT provides a third-order approximation of the non-linear IOD transformation by considering not just the measured values in $\tilde{\boldsymbol{z}}$, but a set of carefully chosen sigma points through the fitting process:

$$(\boldsymbol{X}_E, \mathrm{P}_E) = \mathrm{UT}_{\text{reconstruct}}(\{\mathcal{F}_{\text{IOD}}(\boldsymbol{z}_i, \mathrm{C}_z)\}_{i=1}^{2n_z+1}), \tag{18}$$

where $\boldsymbol{z}_i$ are the sigma points sampled from $\mathcal{N}(\boldsymbol{z}; \tilde{\boldsymbol{z}}, \mathrm{C}_z)$, and $\mathrm{UT}_{\text{reconstruct}}$ is the process in (13). Unlike typical orbital state transformations, where $n = 6$, here the dimension $n_z = 4N$ depends on the track length, potentially becoming much larger. The computational efficiency of the original IOD algorithm makes this approach viable despite the increased dimensionality. This method better captures non-linear effects in the measurement-to-state transformation without requiring explicit higher-order derivatives.

The Taylor algebra method leverages automatic differentiation to compute derivatives through algebraic operations. The function $\mathcal{F}_{\text{IOD}}$ has been implemented in Hipparchus, a programming language supporting this functionality. The result is an enhanced function $\mathcal{F}_{\text{IOD}}^{\mathcal{T}}$ that provides both the state $\boldsymbol{X}_E$ and its derivatives with respect to $\tilde{\boldsymbol{z}}$ up to any desired order. Let us call this combined information the $\boldsymbol{X}_E^{\mathcal{T}}$ Taylor map.

While these derivatives could compute statistical moments as in [1], here the Taylor map $\boldsymbol{X}_E^{\mathcal{T}}$ is directly sampled over the measurements distribution, obtaining a representative point cloud to estimate mean and covariance. Since sampling involves only polynomial evaluations, this method is computationally faster than UT for moderate map orders. This alternative mean-covariance computation is compared against linear and UT methods in subsequent tests.

The output from any IOD method (Linear, Taylor algebra, UT) is compatible with all orbital representations considered in this work. Although the implemented IOD produces Cartesian coordinates directly, transformations described in Section 4.2 may be applied prior to evaluating the detection metric. For the Taylor algebra (TA) method specifically, implementing $T_{\mathcal{A}/\mathcal{B}}^{\mathcal{T}}$ converts the Taylor map $\boldsymbol{X}_E^{\mathcal{T}}$ to the desired representation, after which sampling generates the necessary mean and covariance.

6. COVARIANCE CONSISTENCY VALIDATION

A practical way to check whether a Gaussian approximation remains valid after a general non-linear transformation is to examine the distribution of squared Mahalanobis distances [4, 5]. Let an n-dimensional Gaussian distribution $\mathcal{N}(\boldsymbol{x}; \boldsymbol{\mu}, P)$ be sampled to obtain points $\{\boldsymbol{x}_i\}$. By definition, the quantity

$$k_i^2 \;=\; (\boldsymbol{x}_i - \boldsymbol{\mu})^\mathsf{T}\, P^{-1}\, (\boldsymbol{x}_i - \boldsymbol{\mu})$$

follows a chi-square distribution with n degrees of freedom. Consequently, the sample mean of k_i^2 should be n, and its sample variance $2n$.

After applying any non-linear mapping $f(\cdot)$ to the initial distribution it is convenient to approximate the result by a new Gaussian $\mathcal{N}(\boldsymbol{x}, \boldsymbol{m}, Q)$, which in the context of this work is ever present. If this approximation is consistent with the actual distribution of $f(\boldsymbol{x}_i)$, the new squared Mahalanobis distances

$$\tilde{k}_i^2 \;=\; \big(f(\boldsymbol{x}_i) - \boldsymbol{m}\big)^\mathsf{T}\, Q^{-1}\, \big(f(\boldsymbol{x}_i) - \boldsymbol{m}\big), \qquad (19)$$

should again be distributed approximately as χ_n^2. Therefore, by comparing the empirical distribution of $\tilde{k}_i^2$ with a χ_n^2 reference, one assesses covariance consistency. If the sample statistics (mean, variance) or more formal goodness-of-fit tests reveal large deviations from χ_n^2, the new Gaussian approximation is deemed poor, indicating a breakdown in linearity assumptions. The tests presented in this section serve as preliminary validation of the Gaussian consistency assumption. A more comprehensive assessment of covariance realism is incorporated into the detection metric testing in Section 7, where the practical implications of these assumptions are thoroughly evaluated under operational conditions.

6.1. Prediction covariance consistency

In order to evaluate the propagation methods and state representations from Section 4, a LEO test case is defined with $a = 7000\,\text{km}$ and $e = 0.001$. The initial state distribution employs a position-aligned diagonal covariance in the satellite local frame ($\sigma_r = 20\,\text{m}, \sigma_v = 0.01\,\text{m/s}$), which is then converted to Earth-Centered Inertial coordinates [2] to obtain P_0. The dynamical model follows the *Prediction* dynamics of Table 2, using a numerical propagator from Orekit [18]. A total of 20,000 samples is generated to verify that the initial k_i distribution conforms to a χ^2 law and to observe its subsequent evolution, as illustrated in Figs. 3 and 4.

A graphical assessment of χ^2 consistency is carried out instead of performing formal goodness-of-fit tests. Note

[2]Note that a diagonal covariance in local RSW axes will show correlations between position and velocity after conversion to the inertial frame due to the position dependent velocity of said local frame as defined in [7].

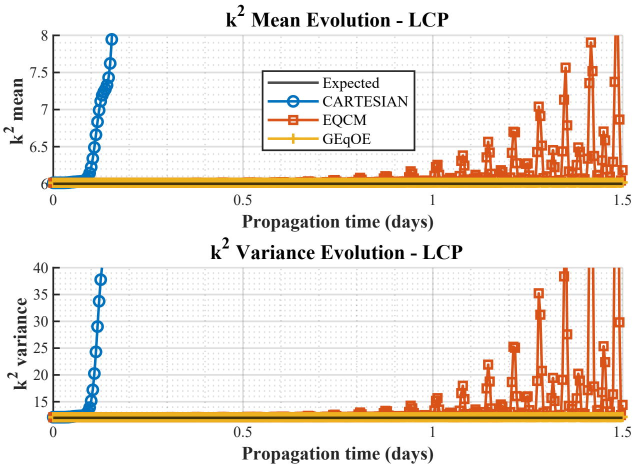

Figure 3. Propagated state k^2 consistency test for three different state representations using LCP method.

that only the Cartesian representation must strictly satisfy the χ^2 behavior at t_0, since the distribution is initially Gaussian in that frame; however, the relatively small initial spread ensures approximate Gaussianity remains valid upon transformation to EQCM and GEqOE.

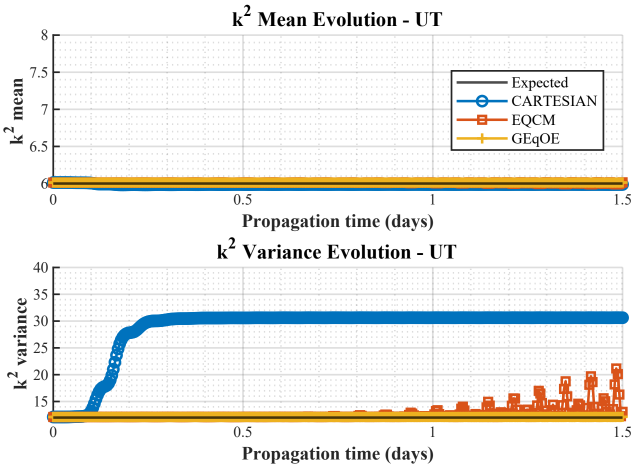

Figure 4. Propagated state k^2 consistency test for three different state representations using UT propagation method.

Focusing on the LCP approach, the Cartesian representation *quickly* breaks the Gaussian assumption—its k^2 mean and variance diverge from the χ^2 expectation in under a quarter of a day. The EQCM representation remains consistent considerably longer (close to a full day) but then also exhibits noticeable deviations. In contrast, the GEqOE-based LCP preserves an almost-Gaussian shape throughout the entire 1.5-day span. This behavior confirms that a simple linear propagation in the Cartesian state can lead to severe overconfidence unless the distribution is kept very small in the first place.

Figure 4 illustrates how the UT further improves consistency of the propagated covariance—especially for non-

Cartesian states—by capturing a wider range of nonlinear effects[3]. Even in Cartesian coordinates, UT-based propagation retains a believable match to the reference χ^2 distribution (albeit with slightly higher variance) for a longer duration than LCP. Unsurprisingly, combining UT with either EQCM or GEqOE yields the best results: they remain close to the χ^2 baseline for nearly the entire simulation, confirming that these more naturally defined orbital coordinates—together with a higher-order propagation technique—can mitigate certain pitfalls of modeling orbital uncertainty as a single Gaussian over extended time intervals.

In conclusion, these numerical checks reinforce that using a curvilinear state representation (EQCM or GEqOE) along with higher-order propagation (e.g., the UT) is preferable for preserving Gaussian consistency over propagation timescales of a day or more. If a strictly linear approach must be used, the GEqOE fare better than the alternatives [16]. This findings are consistent with prior results on the limitations of linearized covariance mappings in orbital mechanics and highlight the benefits of more refined propagation approaches [20].

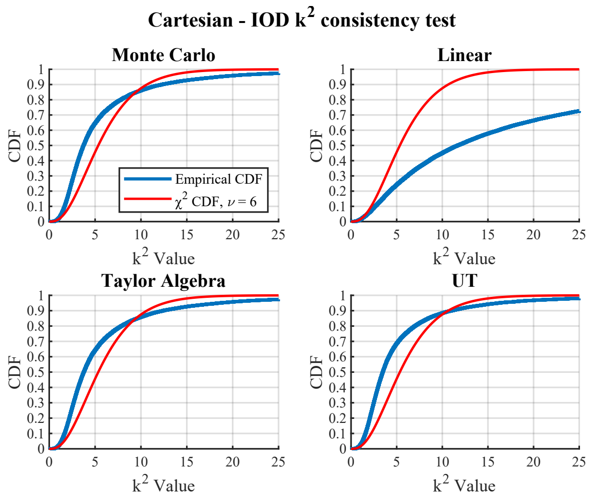

Figure 5. IOD k^2 consistency test for the Cartesian representation using a single track of 6 measurements.

6.2. IOD covariance consistency

The measurement distribution $\mathcal{N}(\boldsymbol{z}; \tilde{\boldsymbol{z}}, \mathrm{C}_z)$ is evaluated through the IOD transformation using each method from Section 5 across all state representations. The $\tilde{k}^2$ distribution (Equation 19) is computed via Monte Carlo (MC) sampling for Linear, Taylor Algebra (TA), and Unscented Transform (UT) methods. Additionally, the mean and covariance of the MC cloud serves as a baseline, representing the optimal Gaussian approximation of the transformed distribution.

[3]The parameters used for the UT in this case are $\alpha = 1/\sqrt{n}$, $\beta = 2$ and $\kappa = 3 - n$

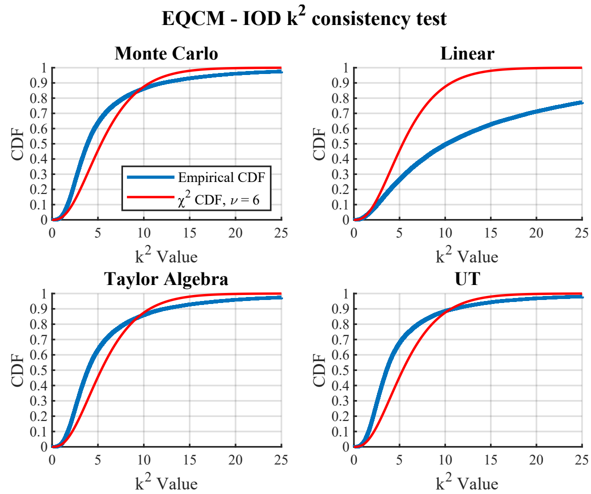

Figure 6. IOD k^2 consistency test for the EQCM representation using a single track of 6 measurements.

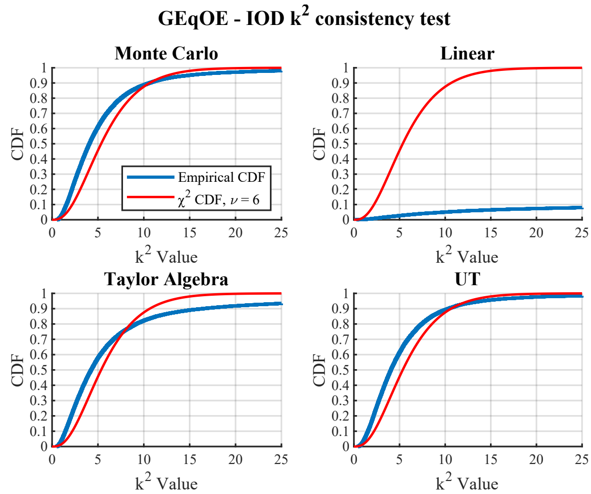

Figure 7. IOD k^2 consistency test for the GEqOE representation using a single track of 6 measurements.

The analysis focuses on short radar tracks where linear approximation typically underperforms [14]. Figures 5, 6, and 7 present results from a simulated six-measurement track with 7-second intervals, using the radar station characterized in Table 4.

Figure 5 confirms the expected underperformance of linear approximation in Cartesian representation. Both TA and UT alternatives demonstrate substantial improvement, approaching the MC baseline performance. Notably, even the MC-derived Gaussian cannot perfectly represent the actual distribution due to inherent nonlinearities. For the UT implementation, parameters $\alpha = 1$, $\beta = 0$, and $\kappa = 0$ yield excellent results regardless of track length, differing from those used in propagation UT (Section 6.1).

The alternative state representations (Figures 6 and 7) also perform adequately with higher-order methods,

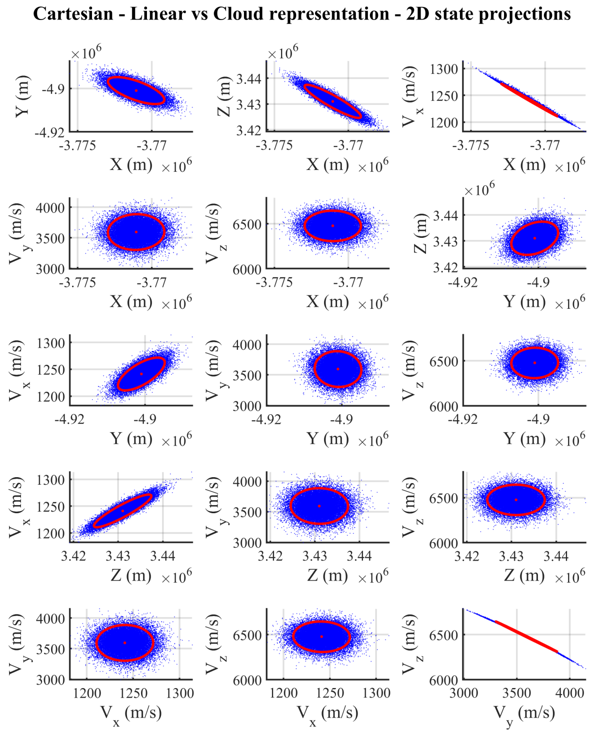

Figure 8. IOD estimation Linear approximation vs full MC representation for Cartesian using a single track of 6 measurements. Every sub-plot is a two component projection of the full state space. Non-linearities are more pronounced in the velocity space.

though TA shows slightly reduced accuracy in GEqOE. Interestingly, the linear approximation in GEqOE performs worst among all alternatives—contrasting with this representation' s excellent performance in uncertainty propagation even with linear covariance propagation. Throughout all tests, the TA method employs a second-order map, providing close approximation to second-order accuracy when using sufficient samples to compute the resulting mean and covariance.

Figures 8, 9 and 10 illustrate the non-linear transformations affecting the measurement distribution, particularly pronounced in GEqOE space. Each sub-plot is a bidimensional projection of the six-dimensional state space, with a total of 15 different combinations. These visualizations qualitatively explain the poor performance of linear approximation methods for short-track IOD processes. While longer track examples are omitted for brevity, it should be noted that non-linearities generally diminish with track length, becoming negligible for tracks of 10 or more measurements.

7. DETECTION METRIC TESTING

This section evaluates the k^2 detection metric' s performance in realistic operational environments where multiple sources of uncertainty coexist: initial state esti-

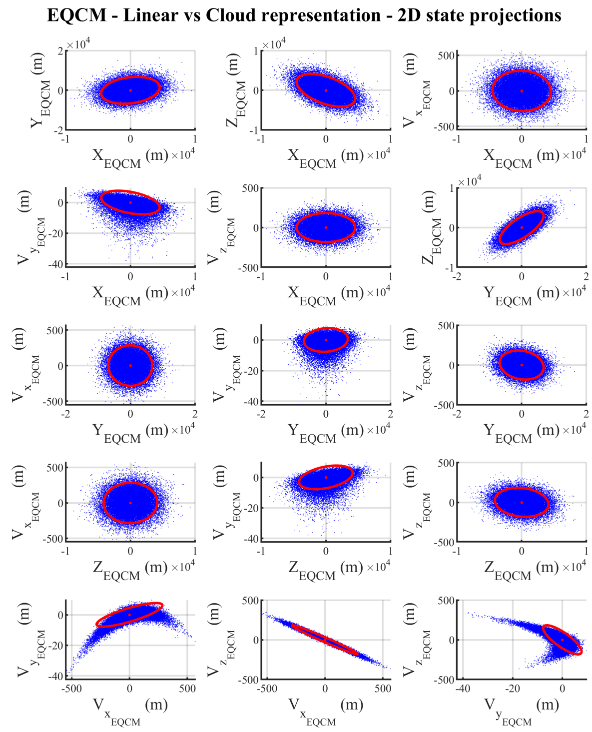

Figure 9. IOD estimation Linear approximation vs full MC representation for EQCM using a single track of 6 measurements.

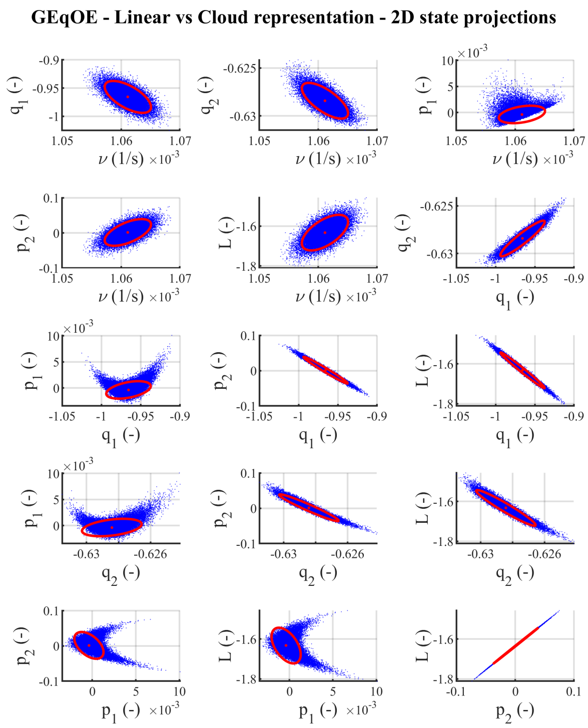

Figure 10. IOD estimation Linear approximation vs full MC representation for the GEqOE using a single track of 6 measurements. Here non-linearities are more generalized among all components.

Table 1. Scenario configuration: orbital and epoch ranges for real satellite state at t_0.

Parameter	Range
Semi-major axis [km]	6900 – 7500
Eccentricity [–]	0.001 – 0.01
Inclination [deg]	40 – 120
RAAN [deg]	0 – 360
Argument of perigee [deg]	0 – 360
Mean anomaly [deg]	0 – 360
Epoch range (YYYY/MM/DD)	2020/01/01 – 2025/01/01

mation, satellite drag modeling, dynamical environment, and measurement noise. The testing systematically examines the metric against low-magnitude maneuvers (as small as 2 cm/s) to establish practical detection limits and reliability boundaries.

The reliability of detection methods—specifically their false positive rates—is the primary focus. A properly calibrated metric with a detection threshold set at confidence level $(1-\delta)$ should exhibit false positive rates not exceeding δ. When empirical false positive rates consistently exceed this threshold, it indicates violation of underlying assumptions (particularly Gaussianity) and invalidates statistical confidence in detection outcomes.

Through comprehensive testing across varied orbital regimes and track lengths, this section establishes concrete guidelines for applying different state representations and uncertainty propagation methods to maximize both sensitivity and reliability in operational scenarios.

7.1. Simulated scenario design

The testing framework incorporates variability across parameters that influence detection metrics. At a high level, a *scenario* encompasses a range of orbital regimes, as shown in Table 1, with the lowest altitude at approximately 453 km—well within the region of significant atmospheric perturbation.

From this scenario, multiple test *cases* are generated, each defined by a specific orbital state sampled from the scenario' s parameter space. These cases produce one synthetic radar track through "high-fidelity" trajectory simulation using the *Real* dynamics model described in Table 2. The satellite is modeled using a cannonball approach with parameters specified in Table 3, which defines the cross-sectional area, mass, and drag coefficient used in the atmospheric and solar radiation pressure perturbations. By construction of the sampling, a subset of cases (70% of the total population) includes an impulsive prograde maneuver with magnitude $\Delta V \in [2, 35]$ cm/s, while the remaining 30% represent non-maneuvered cases used to validate false positive rates.

To introduce realistic uncertainty in the testing process, each case incorporates variability in multiple dimensions.

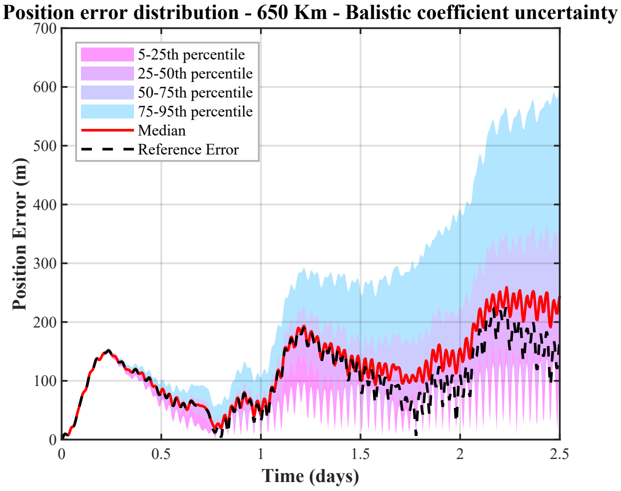

Figure 11. Monte Carlo of the position error distribution when only the satellite' s model uncertainty is introduced in simulation against the ground truth (Real vs Simulated dynamics) for a 650 Km orbit.

Both the *real* satellite and the *perfect* radar measurements are sampled to generate the measurement distribution $\mathcal{N}(\boldsymbol{z}; \tilde{\boldsymbol{z}}, \mathrm{C}_z)$, the state prior estimate $\mathcal{N}(\boldsymbol{x}; \boldsymbol{X}_0, \mathrm{P}_0)$, and the ballistic coefficient $\boldsymbol{p}$.

The radar measurements are sampled using the uncertainty values specified in Table 4, producing both the observed values $\tilde{\boldsymbol{z}}$ and their associated covariance matrix C_z. The initial satellite state and ballistic coefficient are sampled using standard deviations shown in Table 3. For these tests, the initial state uncertainty is defined by position and velocity standard deviations of $\sigma_r = 10\,\mathrm{m}$ and $\sigma_v = 0.005\,\mathrm{m/s}$ respectively in the satellite local frame, which are then converted to the inertial frame to compute P_0 and $\boldsymbol{X}_0$ from it. This approach ensures that neither the initial state estimate $\boldsymbol{X}_0$ nor the parameters $\boldsymbol{p}$ used for prediction exactly match the real satellite. The subsampling within each case is repeated 50 times, and the metric computed in each of those *experiments*, to provide statistical significance to the results.

As explained in Section 4.1, only the uncertainty in the initial conditions is accounted for when estimating the satellite' s state distribution at t_{ref}. The discrepancies in both the dynamics (*Prediction* model in Table 2) and the satellite ballistic coefficient introduce systematic biases that depend primarily on the atmospheric perturbation' s relative importance. Figures 11 and 12 illustrate the position error distributions resulting from these combined uncertainties (dynamics and ballistic coefficient) at two different orbital altitudes. The reference error represents the deviation between Prediction and Real dynamics when using identical satellite parameters $\boldsymbol{p}$ and initial state $\boldsymbol{X}_0$. This testing approach deliberately introduces deviations from the core assumption of supposed covariance realism, as the propagation step does not account for these discrepancies, allowing evaluation of their effect directly on metric performance.

Table 2. The two dynamical models defined, one for the real trajectory and another for predictions. SRP stands for Solar Radiation Pressure.

Model	Earth harmonics	Atmosphere	Sun	Moon	SRP
Real	[10, 10]	Harris-Priester	yes	yes	yes
Prediction	[9, 9]	Harris-Priester	no	no	no

Table 3. Satellite model and uncertainty parameters. The position/velocity (r and v) standard deviations are defined in local RSW axis (position-oriented).

Parameter	Value
Mass [kg]	420
Cross-sectional area S [m^2]	4
Drag coefficient C_D	2.3000
SRP area [m^2]	4
σ_{mass} [kg]	1.41
σ_{C_D}	0.09
σ_r [m]	10
σ_v [m/s]	0.005

Table 4. Characterization of simulated radar, Field of Regard is omitted.

Parameter	Value
(λ, ϕ) (°)	$(-5.59, 37.17)$
h (m)	142.32
σ_ρ (m)	7
$\sigma_{\dot\rho}$ (m/s)	0.4
σ_{Az} (°)	0.3
σ_{el} (°)	0.2
$\xi_{\text{Az,el}}$	0.043
r_t (s)	7

Figure 13 presents the distribution of key parameters across the experimental population. Some parameters follow the intended design constraints, such as orbital elements and impulse magnitudes, which were generated with uniform probability distributions. Other parameters, particularly simulation duration, exhibit distributions that emerge as consequences of the scenario configuration. These emergent distributions primarily result from the interaction between radar placement and orbital altitudes, where higher orbits demonstrate increased probability of entering the radar' s Field of View (FoV).

7.2. Statistical results of k^2 metrics

For the results presented in this document, the LCP method for uncertainty propagation has been excluded for conciseness. All k^2 metrics employ the Unscented Transform (UT) for prediction computation, as it provides a more conservative approach. Of particular importance is the selection of the reference state when using the EQCM representation. In all cases the default reference frame is that of the IOD estimate, as it is typically the one with

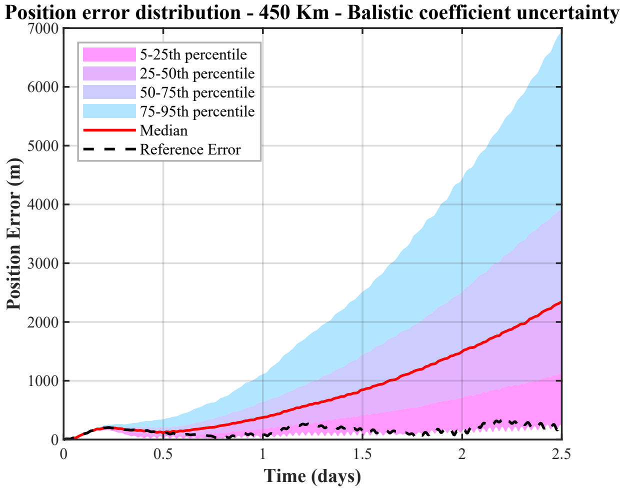

Figure 12. Monte Carlo of the position error distribution when only the satellite' s model uncertainty is introduced in simulation against the ground truth (Real vs Simulated dynamics) for a 450 Km orbit.

less uncertainty.

Each k^2 evaluation experiment yields only two relevant outcomes for this analysis. When the metric value exceeds the threshold defined in Equation 6, the result is classified as a Detection (True Positive) in maneuver cases, or as a False Positive otherwise. Complementary results (False Negatives or True Negatives) are not explicitly presented. Therefore, Detection percentages represent the proportion of correctly identified maneuvers relative to the total number of maneuvered cases under consideration (subject to parameter-specific filtering). Similarly, False Positive percentages reflect the proportion of incorrectly identified maneuvers among non-maneuvered cases.

The more general statistics can be found in Table 5. Each row includes the results by state representation (which is by definition the same in both prediction and IOD), while each column corresponds to the method used in the IOD step. Note that these have been computed at 95% confidence level, indicating that the theoretical or expected rate of False positives should not exceed 5% if all basic assumptions presented in Section 3 are met. In that note, the first analysed outcome should always be the False Positives, as this is the main indicator of reliability.

Examination of the Cartesian results reveals only marginal advantages for the UT-based IOD method compared to alternatives, with improvements insufficient to

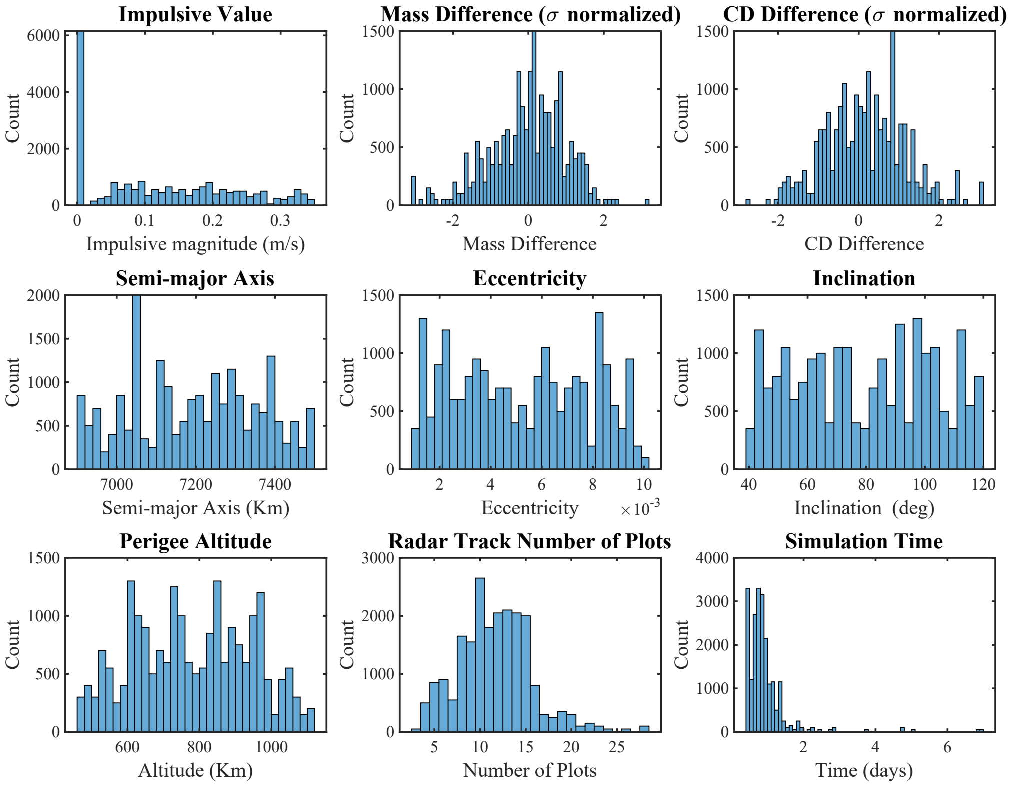

Figure 13. Histograms depicting the distributions of key experimental parameters on the scenario used for Section 7.2 results. Each subplot shows the frequency distribution for a specific variable.

establish any method as reliable. Contrary to expectations, EQCM demonstrates inferior performance, exhibiting an approximately 3% elevation in false positive rates across all scenarios. The GEqOE framework, however, presents promising alternatives, with both UT and Taylor algebra approaches achieving performance metrics approximating optimal outcomes.

These systematic underperformances were expected, as the employed propagation methodology does not account for model discrepancies or inaccuracies in the satellite' s dynamic environment. This limitation leads to overly optimistic covariance estimates and consequently unrealistic predictions. The results support the hypothesis that the k^2 metric tends to misclassify non-maneuvered cases due to overconfident covariance propagation and inadequate representation of dynamical divergence between the predicted and true trajectories. In this context, the strong performance exhibited by the GEqOE representation is particularly noteworthy.

A comprehensive explanation of these results necessitates statistical analysis as a function of key scenario parameters. The atmospheric perturbation emerges as a primary contributor to prediction errors within this scenario. Figure 14 confirms this relationship, revealing pronounced spikes in False Positive rates for both Cartesian and EQCM representations at lower altitudes. The apparent immunity of GEqOE to these effects likely stems from two complementary factors.

First, as demonstrated in Figure 4, the GEqOE orbital representation maintains covariance consistency substantially longer than alternative formulations, suggesting enhanced resilience to dynamics mismodeling. Second, the detection metric is significantly influenced by the IOD methodology itself. The observed performance may result from compensatory effects in the UT and Taylor algebra approaches when characterizing error distributions, which effectively counterbalance divergence in the prediction component.

A more rigorous investigation into these results, particularly regarding the covariance realism properties across different state representations, remains essential for developing a definitive analysis of these phenomena.

The sensitivity to maneuver detection merits detailed consideration exclusively in the context of GEqOE, as it represents the only alternative exhibiting close correspondence with expected False Positive rates (when excluding the linear method from consideration). Figure 15 indicates that maneuvers exceeding 15-50 cm/s consistently trigger the detection threshold, demonstrating the sensitivity of this methodology when employing an optimal combination of orbital state representation and IOD method. These significant performance improvements are attributable directly to the incorporation of higher-order approximations in the IOD calculation process, extending beyond conventional linear approaches.

Table 5. Detection and False Positive rates by orbital representation and IOD Method (95% Confidence Level) for all test cases.

	Linear		UT		Taylor Algebra	
Representation	Detection (%)	False Positive (%)	Detection (%)	False Positive (%)	Detection (%)	False Positive (%)
Cartesian	95.70	20.61	93.61	15.82	95.69	20.54
EQCM	95.92	23.07	94.01	18.21	95.85	23.16
GEQOE	96.65	43.79	83.73	8.57	84.53	9.39

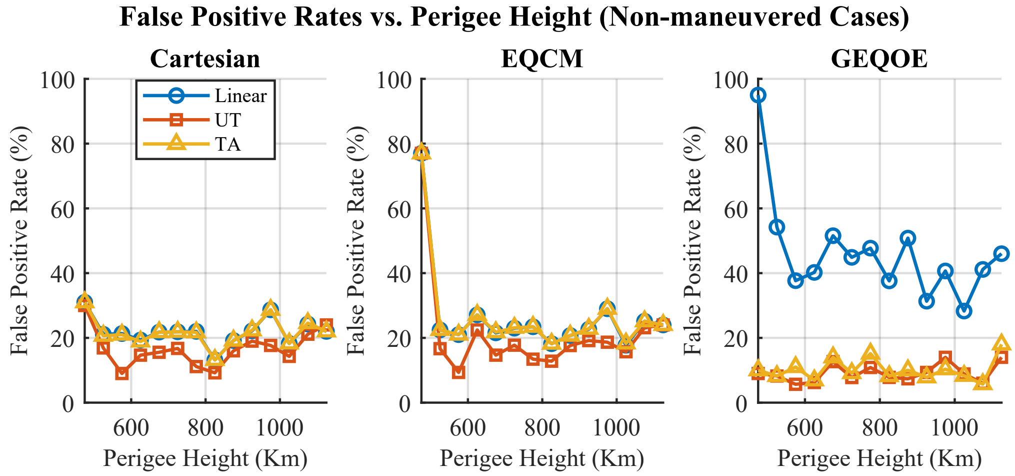

Figure 14. False positives rates for the three orbital representations and IOD methods with the perigee height. Each data point corresponds to a 50 Km interval from 450 Km.

8. CONCLUSIONS

This work has demonstrated that the effectiveness of maneuver detection metrics in LEO surveillance operations significantly depends on both state representation and uncertainty propagation methods. Our comprehensive testing reveals that Generalized Equinoctial Orbital Elements (GEqOE) substantially outperform both Cartesian and EQCM representations in maintaining Gaussian consistency during extended propagation periods. When combined with the Unscented Transform or Taylor algebra methods for Initial Orbit Determination, GEqOE enables reliable detection of maneuvers as small as 15-20 cm/s while maintaining false positive rates near theoretical expectations (8-9% versus the theoretical 5% at 95% confidence).

Particularly notable is GEqOE' s resilience to altitude-dependent atmospheric perturbation effects that severely compromise both Cartesian and EQCM approaches. Additionally, advanced IOD techniques—especially UT-based methods—offer substantial improvements over traditional linear methods, particularly for short radar tracks where non-linearities dominate measurement-to-state mapping.

These findings provide practical guidelines for operational implementations: maneuver detection in LEO environments should employ GEqOE representation with UT-based uncertainty propagation, complemented by either UT or Taylor algebra for IOD processing. Future work should focus on further improving uncertainty realism by explicitly accounting for dynamical model discrepancies, which remain the primary limitation of the current approach.

ACKNOWLEDGMENTS

The authors gratefully acknowledge support by grant TED2021-132099B-C33 funded by MICIU/ AEI/ 10.13039 /501100011033 and by "European Union NextGenerationEU/PRTR." Jose M. Montilla acknowledges the support from Universidad de Sevilla under VI PPIT-US.

REFERENCES

1. Armellin, R., & Di Lizia, P. (2018). Probabilistic optical and radar initial orbit determination. *Journal of Guidance, Control, and Dynamics*, *41*(1), 101–118. American Institute of Aeronautics and Astronautics.
2. A. Pastor, M. Sanjurjo-Rivo, and D. Escobar, *Initial orbit determination methods for track-to-track association*, *Advances in Space Research*, vol. 68, no. 7, pp. 2677–2694, 2021.
3. A. D. Jaunzemis, M. V. Mathew, and M. J. Holzinger, *Control Cost and Mahalanobis Distance Binary Hy-*

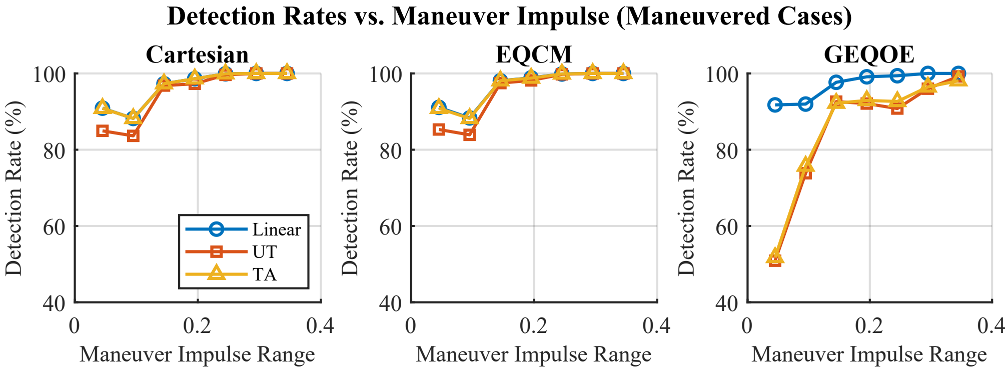

Figure 15. Detection rates for the three orbital representations and IOD methods with the impulse value. Each data point corresponds to a 3 cm/s inverval starting at 2 cm/s.

pothesis Testing for Spacecraft Maneuver Detection, *Journal of Guidance, Control, and Dynamics*, vol. 39, no. 9, pp. 2058–2072, 2016.

4. A. Cano, A. Pastor, D. Escobar, J. M'ıguez, and M. Sanjurjo-Rivo, *Covariance determination for improving uncertainty realism in orbit determination and propagation*, *Advances in Space Research*, vol. 72, no. 7, pp. 2759–2777, 2023.
5. B. Reihs, A. Vananti, T. Schildknecht, J. A. Siminski, and T. Flohrer, "Application of attributables to the correlation of surveillance radar measurements," *Acta Astronautica*, vol. 182, pp. 399–415, 2021.
6. D. C. Easley and T. Berry, *A higher order unscented transform*, *SIAM/ASA Journal on Uncertainty Quantification*, vol. 9, no. 3, pp. 1094–1131, 2021.
7. D. A. Vallado, *Covariance transformations for satellite flight dynamics operations*, *Advances in the Astronautical Sciences*, vol. 116, pp. 1–35, 2004.
8. G. Escribano, M. Sanjurjo-Rivo, J. A. Siminski, A. Pastor, and D. Escobar, *Automatic maneuver detection and tracking of space objects in optical survey scenarios based on stochastic hybrid systems formulation*, *Advances in Space Research*, vol. 69, no. 9, pp. 3460–3477, 2022.
9. G. Baù, J. Hernando-Ayuso, and C. Bombardelli, *A Generalization of the Equinoctial Orbital Elements*, Celestial Mechanics and Dynamical Astronomy, vol. 133, pp. 1–29, 2021, Springer.
10. G. M. Goff, *Orbit Estimation of Non-Cooperative Maneuvering Spacecraft*, PhD thesis, Air Force Institute of Technology, 2015.
11. D. A. Vallado and S. Alfano, *Curvilinear Coordinate Transformations for Relative Motion*, Celestial Mechanics and Dynamical Astronomy, vol. 118, no. 3, pp. 253–271, 2014, Springer.
12. J. M. Montilla, R. Vazquez, and P. Di Lizia, *Maneuver Detection with Two Mixture-Based Metrics for Radar Track Data*, *Journal of Guidance, Control, and Dynamics*, pp. 1–17, 2025.
13. J. M. Montilla, *Satellite Maneuver Detection with Radar Data: Leveraging Improved Orbital Uncertainty Characterization for Reachability-Based Metrics*, PhD thesis, Universidad de Sevilla, 2024.
14. J. M. Montilla, J. A. Siminski, and R. Vázquez, *Single Track Orbit Determination Analysis for Low Earth Orbit with Approximated J2 Dynamics*, Advances in Space Research, vol. 74, no. 10, pp. 4968–4989, 2024, Elsevier.
15. J. M. Montilla, J. C. Sanchez, R. Vazquez, J. Galan-Vioque, J. R. Benayas, and J. Siminski, *Manoeuvre detection in Low Earth Orbit with radar data*, *Advances in Space Research*, vol. 72, no. 7, pp. 2689–2709, 2023.
16. J. Hernando-Ayuso, C. Bombardelli, G. Ba'u, and A. Mart'ınez-Cacho, *Near-linear orbit uncertainty propagation using the generalized equinoctial orbital elements*, *Journal of Guidance, Control, and Dynamics*, vol. 46, no. 4, pp. 654–665, 2023.
17. J. Siminski, T. Flohrer, and T. Schildknecht, *Assessment of post-maneuver observation correlation using short-arc tracklets*, *Journal of the British Interplanetary Society*, vol. 70, pp. 63–68, 2017.
18. L. Maisonobe, V. Pommier, and P. Parraud, *Orekit: An open source library for operational flight dynamics applications*, in *4th International Conference on Astrodynamics Tools and Techniques*, European Space Agency, Paris, 2010, pp. 3–6.
19. M. J. Holzinger, D. J. Scheeres, and K. T. Alfriend, *Object correlation, maneuver detection, and characterization using control distance metrics*, *Journal of Guidance, Control, and Dynamics*, vol. 35, no. 4, pp. 1312–1325, 2012.
20. A. B. Poore, J. M. Aristoff, J. T. Horwood, R. Armellin, W. T. Cerven, Y. Cheng, C. M. Cox, R. S. Erwin, J. H. Frisbee, M. D. Hejduk, *et al.*, *Covariance and uncertainty realism in space surveillance and tracking*, Tech. Rep., Numerica Corporation, Fort Collins, United States, 2016
21. R. A. Broucke and P. J. Cefola, *On the Equinoctial Orbit Elements*, Celestial Mechanics, vol. 5, no. 3, pp. 303–310, 1972, Springer.
22. X. R. Li and V. P. Jilkov, *Survey of maneuvering target tracking. Part V. Multiple-model methods*, *IEEE Transactions on Aerospace and Electronic Systems*, vol. 41, no. 4, pp. 1255–1321, 2005.